Research Square

Preprints are preliminary reports that have not undergone peer review.
They should not be considered conclusive, used to inform clinical practice,
or referenced by the media as validated information.

Scaffolding Protein Mimics Using a DNA Nanostructure

Hanadi Sleiman

hanadi.sleiman@mcgill.ca

McGill University https://orcid.org/0000-0002-5100-0532

Fangzhou Zhao

McGill University

Tianxiao Yang

McGill University

Daniel Saliba

McGill University

Trishalina Das

McGill University

Jathavan Asohan

McGill

Alba Guarné

McGill University https://orcid.org/0000-0003-4906-9132

Article

Keywords:

Posted Date: June 4th, 2026

DOI: https://doi.org/10.21203/rs.3.rs-7348237/v1

License: This work is licensed under a Creative Commons Attribution 4.0 International License.
Read Full License

Additional Declarations: There is **NO** Competing Interest.

Scaffolding Protein Mimics Using a DNA Nanostructure

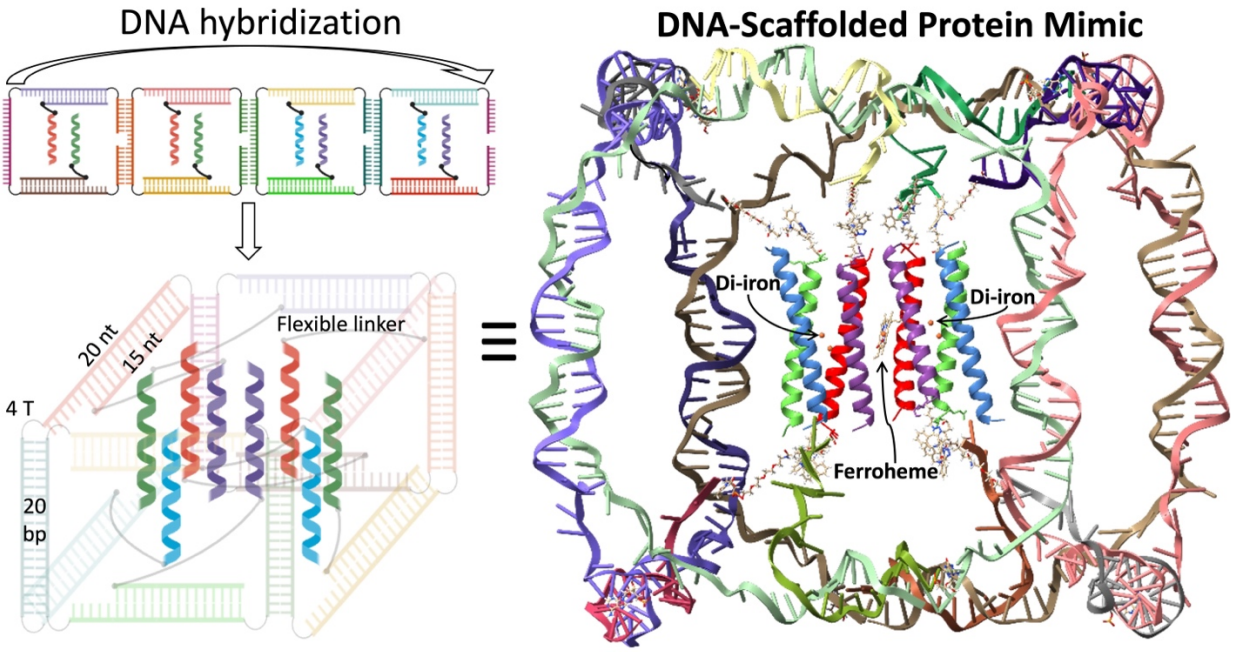
Fangzhou Zhao[a], Tianxiao Yang[b], Daniel Saliba[a], Ziyi Sun[a], Trishalina Das[a], Jathavan Asohan[a], Yihao Wu[a], Alba Guarné[b], and Hanadi F. Sleiman[a]*

[a]Department of Chemistry and Centre de Recherche en Biologie Structurale, McGill University, 801 Sherbrooke St. W., Montreal, QC, Canada

[b]Department of Biochemistry and Centre de Recherche en Biologie Structurale, McGill University, Montreal, QC, Canada

*E-mail: hanadi.sleiman@mcgill.ca

Abstract



Recent advances in protein engineering have resulted in breakthroughs in structure prediction, functional material development and drug discovery. To expand the current toolbox, DNA nanostructures offer an orthogonal and programmable platform for scaffolding peptide assembly.

Here, we use a three-dimensional DNA cube to organize short peptides into a functional bacterioferritin active site-mimic, with precise control over peptide sequence, orientation, and composition at the nanometer scale. Each component is individually addressable, enabling rapid sequence swapping and dynamic function switching via DNA strand displacement. The assemblies reproduce native functionalities - heme binding, iron oxidation, and radical stabilization - and further assemble into higher-order complexes. Site-specific substitution of metal-coordinating (H17N, E14L) and heme-binding (M15L) residues abrogates iron oxidation and modulates heme binding, directly confirming that functionality originates from the designed active site. This strategy establishes a versatile platform for high-throughput exploration of structural variants, including non-natural subunit orientation and multivalent architectures with tunable properties.

Introduction

Nature has evolved proteins to regulate life's fundamental functions in diverse and elegant ways. By unraveling the principles of protein folding, recent studies have discovered key interactions that enable the design of novel protein structures with unique geometries and functions.[1-4] Breakthroughs in protein engineering by machine-learning methods, such as AlphaFold[5] and RFdiffusion,[6-8] have greatly accelerated the prediction and design of protein structures. Deep-learning models are typically trained on crystallized protein structures and can generate predictions that deviate from actual conformations in solution, especially for and conformationally flexible proteins.[9, 10] On the number of amino acid residues, and the incorporation of non-canonical or artificial units remains difficult. On the experimental side, expressing and purifying large numbers of protein variants can be resource-intensive, as a single residue change often necessitates

resynthesis of the entire protein chain. Approaches that can incorporate non-canonical or artificial subunits at defined positions, enable stimuli-responsive function, and allow high-throughput exploration of multicomponent sequence space, would complement these powerful frameworks considerably.

These considerations motivate the development of alternative bottom-up strategies to construct protein mimics. Scaffolded protein assembly can offer a route to protein engineering, in which synthetic peptide fragments are organized on templates with pre-defined geometries, to form higher-order architectures.[11, 12] Chemical peptide synthesis is intrinsically compatible with the incorporation of artificial units and would allow modular design, generating structural variants by replacing only essential components to modulate the architecture. An ideal scaffold should organize peptide building blocks into defined geometries, while minimizing unwanted interactions that could lead to misfolding or aggregation. To this end, researchers have employed synthetic molecules[13-18] and protein motifs[6, 19-25] as scaffolds. However, synthetic templates are often inherently symmetrical, and achieving defined asymmetry for precise multivalent presentation typically requires complex synthetic routes.[26-30] Protein-based scaffolds, on the other hand, often require the target modules to be incorporated into the same polypeptide chain. This introduces challenges in recombinant expression and misfolding due to unwanted interactions between target and scaffold motifs. Iterative design and experimental optimization are therefore often required.[31-35]

DNA nanotechnology can offer uniquely programmable scaffolds that operate orthogonally to protein chemistry.[36-39] By exploiting Watson-Crick-Franklin base-pairing, it is possible to assemble three-dimensional structures with arbitrary shapes, capable of precisely positioning various materials at the nanoscale.[40] DNA nanostructures can be further expanded into higher-order

assemblies, and endowed with dynamic behavior: strand-displacement reactions, for example, allow parts of the structure to rearrange or unlock in response to specific triggers.[41] Proof-of-concept studies from our laboratory showed that a simple trimeric DNA motif can organize short peptides into coiled-coil bundles[42] and metalloprotein mimics.[43] Three-dimensional DNA nanostructures would extend this strategy to the construction of functional enzyme mimics (**Figure 1A**). In this approach, an enzyme can be reduced to its essential active-site peptide elements, each tethered to a distinct DNA strand; upon hybridization to a predefined scaffold, these fragments are arranged with nanometer-scale precision. Fine conformational optimization can then be achieved by the preserved peptide-peptide and peptide-ligand interactions on such scaffolds, reconstructing native active site chemistry without requiring full complex folding pathways. Mutations can be introduced by swapping peptide units, without disrupting the local structure. This modularity provides a systematic route to explore and optimize peptide function, which that would be difficult to achieve with contiguous protein chains. DNA-templated protein mimic assembly also allows the introduction of non-canonical modifications, new catalytic functions, and stimuli-responsive behaviour that are difficult to achieve by conventional protein engineering.

Here, we report a DNA cube-scaffolded assembly strategy to recapitulate the functional site of bacterioferritin (Bfr, **Figure 1**)[44] using short synthetic peptide fragments. The DNA nanocube is assembled from four clip strands, each hybridized to two DNA-peptide conjugates (Clip, **Figure 1B**). This preorganized DNA template enables the assembly of eight short peptide fragments into a Bfr subunit mimic (**Figure 1C**). The DNA scaffold provides structural support with minimal interference with the functional peptide domains and endows them with broad mutational tunability, from unnatural primary sequences to diverse subunit orientations, without compromising structural integrity. Exploring these unnatural configurations offers unique insights

into sequence-structure-function relationships of the native enzyme. Because each peptide fragment can be individually addressed, the composition and catalytic activity of the resulting protein mimic can be precisely regulated by stimuli-responsive DNA strand displacement pathways. Beyond dynamic control at the single assembly level, the modularity of DNA scaffolding also enables hierarchical organization of peptide subunits. Appending DNA overhangs directs the assembly of cube-protein mimics onto a spherical nucleic acid (SNA), forming higher -order protein mimic-micelle complexes, in a single mixing step with high efficiency and yield. This hierarchical assembly increases the local density of catalytic subunits, enhances catalytic activity, and recapitulates key architectural features of natural multimeric protein cages. This work introduces a 3D DNA-scaffolded enzyme mimic assembled entirely from synthetic strands, in which the orthogonal language of DNA base pairing operates alongside peptide assembly to create a programmable, modular framework for regulating structure and function with high precision and reliability.

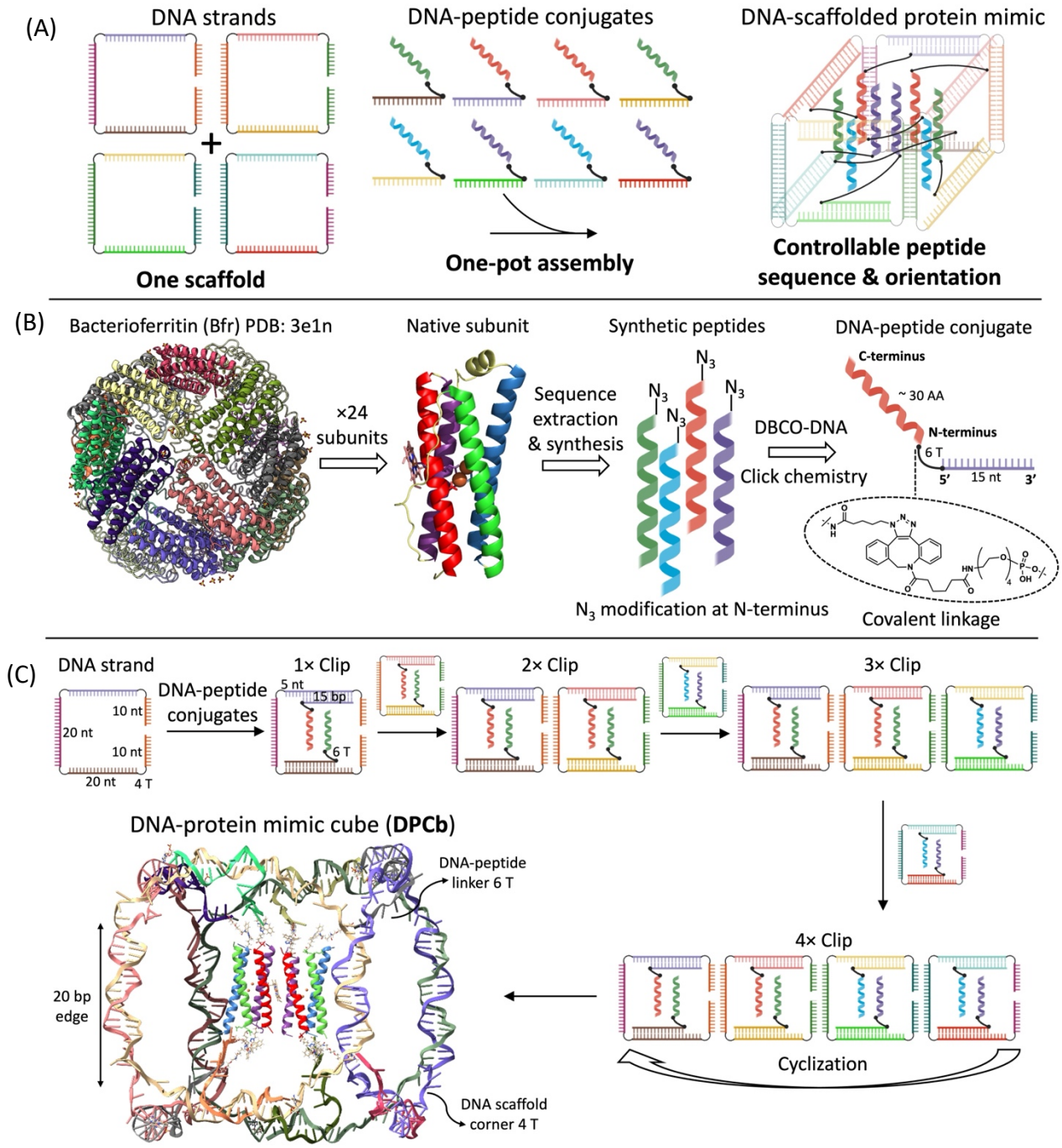


Figure 1. Design and assembly of DNA-protein mimics. (A) Schematic representation of the assembly of protein mimic scaffolded by a DNA cube. (B) Design and assembly of DNA-protein mimic cube. Peptide sequences (BF1-4), corresponding to helices A-D of the *E. coil* bacterioferritin (Bfr) subunit (**Table S2**),[45, 46] were produced by solid-phase peptide synthesis (SPPS) with N_3 modification at the N-terminus. Peptides were conjugated to DBCO-DNA covalently by copper-free click chemistry (details in **SI-VI**). The resulting DNA-peptide conjugates were assembled into protein mimics scaffolded by DNA cube (details in **SI-VII**). (C) Structural model of the DNA-protein mimic cube (DPCb). The DNA scaffold was generated by molecular dynamics (MD) simulation using OxDNA,[47] and polypeptide conformations were predicted using AlphaFold.[5] The combined model was assembled and visualized in PyMOL[48] and ChimeraX.[49]

Results and Discussion

Protein Mimic Design

Bacterioferritin (Bfr),[50] is a nearly spherical protein assembled from 24 identical subunits and 12 hemes, playing a vital role in iron homeostasis. Each subunit contains a di-iron binding site located within its four-helix bundle, and each heme is positioned at the interface between two neighboring subunits through Met-heme-Met interactions.[44] Dimeric Bfr subunits serve primary intermediate in the spontaneous self-assembly of the full 24-mer oligomer.[51] The minimal building block preserves both the interfacial heme binding site and the metal-binding sites within each helical bundle,[52, 53] making it an attractive model for probing structural and functional aspects of the native protein. However, isolation of Bfr dimers has typically relied on dissociation of the native oligomer under non-physiological conditions,[54, 55] or on site-directed mutagenesis to disrupt the higher-order assembly.[56, 57] DNA-scaffolded assembly offers a bottom-up alternative: individual subunits are organized with defined geometry, providing direct control over peptide orientation and oligomeric state.

To construct the protein mimic, we extracted the functional peptide sequences from the native helical bundle by excising the flexible linkers connecting the helices (**Figure 1B**, synthetic peptides). The resulting peptide fragments were produced using solid-phase synthesis, and their N-termini were modified with an azide functional group (**Table S2**, BF1-4). They were subsequently conjugated to DBCO-DNA strands via strain-promoted-copper-free click reaction[58] (**Figure 1B**, DNA-peptide conjugate). Because the DNA and peptide components are synthesized independently, their sequences and lengths can be varied freely to control geometry and subunit composition. It is of note that both functionalized peptides and DNA strands can be commercially

obtained, making this strategy accessible to all labs. Following a strategy previously developed in our group,[59] we constructed a three-dimensional DNA cube to scaffold the protein mimic. The cube consists of four "clip" strands and presents eight single-stranded edges, which can hybridize with diverse functional components, including gold nanoparticles,[60] siRNA,[61] and polymer particles.[62] Each clip strand hybridizes with two DNA-peptide conjugates to form a DNA-peptide clip (1× Clip, **Figure 1C**). Additional clips are sequentially introduced and joined through hybridization (2-4× Clip, **Figure 1C**). This cube is completed by cyclizing the terminal edge of the fourth clip with the complementary starting edge of the first clip (DPCb, **Figure 1C**). This modular, asymmetric assembly spatially organizes all eight peptide subunits within the scaffold. By varying the assembly components, DNA cages with distinct subunit oligomeric states and orientations, peptide sequences, and structural properties can be readily constructed in high yield (**SI-VII**).

Cube-Scaffolded Assembly of Protein Mimics

The DNA cube provides a programmable structural framework, while fine conformational adjustment is driven by peptide-peptide interactions, when appropriate linker length and scaffold flexibility are present. As shown by the atomic model of DNA-protein mimic cube (**Figure 2A**, DPCb), the distances between the scaffolding DNA edges and peptide termini are expected to be around 5-6 nm. To ensure sufficient length for the anchored peptides to interact with each other (**Figure S1**), a six-thymidine (6T) linker was incorporated between the DNA and peptide (**Figure 2A**, DNA-peptide conjugates). Previous studies from our laboratory showed that this cube scaffold is flexible enough to allow hydrophobic units to assemble intramolecularly into a hydrophobic environment on its inside.[62-65] We hypothesized that a similar intramolecular "handshake" can occur between the encapsulated peptides in the cube scaffold, strengthened by peptide-peptide

interactions. DPCb was assembled by mixing eight DNA-6 T-peptide conjugates with the four clip strands in a one-pot annealing manner. The resulting constructs showed a single, well-defined band on native agarose gel electrophoresis (AGE, **Figure 2B**) and discrete nanostructures by atomic force microscopy (AFM, **Figure 2C**). Dynamic light scattering (DLS) analysis indicated that DPCb had a hydrodynamic diameter of 10.8 nm, approximately 3 nm smaller than its DNA-only cube (13.8 nm), with a comparable polydispersity index (PDI ≈ 0.3, **Figure 2D**). Circular dichroism (CD) characterization showed a negative band at 206 nm, suggesting the presence of helical secondary structure (**Figure 2E**, orange; CD spectra are reported after subtraction of the corresponding DNA-only cube spectrum at equivalent strand concentration). Together, these results support a model in which the peptide fragments assemble within the interior of the cube rather than extending outward from the scaffold (see below for further evidence).

The DNA cube allows the assembly of peptides at sub-micromolar concentrations by increasing their local concentration. In contrast, without DNA scaffolding, peptide assembly is driven primarily by bulk concentration. CD spectra (**Figure S11A**) showed that the same peptides failed to form organized secondary structures even at 50 μM each (peptide BF1-4), as evidenced by a random coil conformation. At a higher concentration of 150 μM per peptide, a negative band at 205.5 nm with lower mean residue ellipticity intensity was observed (**Figure 2E**, green), suggesting that the secondary structure is still relatively limited. In addition, DLS (**Figure 2D**, green) and AFM imaging (**Figure S9G**) revealed that the peptide mixtures formed large particles with ~30 nm size and poor dispersity (PDI > 0.7). Considering that each peptide is only 30 amino acids in length, these particles likely contain hundreds of peptide strands with random oligomeric states. This comparison highlights the precision and programmability of DNA scaffolding in promoting peptide-peptide interactions while providing structural control.

The programmability of DNA nanostructures also makes structural modifications straightforward, and unlocks the possibility to explore architectures with variable features on demand. Because each component can be addressed individually, specific properties can be tuned by adjusting only the required strands, without disrupting the overall assembly. Taking advantage of this, we first examined the role of linker length. The same azido-peptides were directly conjugated to DBCO-DNA without additional spacers. The resulting short DNA-peptide conjugates were assembled with the same cube scaffold (**Figure 2F**), yielding a three-dimensional structure (sDPCb, **Figure 2G**) that also displayed a clean band on native AGE (**Figure 2H**). However, CD spectra revealed a predominantly random coil conformation with a negative peak at 202 nm (**Figure S12A**, yellow). While the DNA-only cube exhibited a smaller diameter of 11.1 nm and improved monodispersity by DLS (PDI = 0.31, **Figure S22A**, blue), DLS characterisation of the DNA-peptide cube sDPCb showed a hydrodynamic diameter of 13.3 nm and a more disperse PDI of 0.52 (**Figure S22A**, yellow). The size increase and higher PDI of sDPCb (**Figure 2D**, yellow vs orange) suggests that the peptides are not properly assembled within the interior of the cube, but instead extend outward from the scaffold.

After validating the linker length, we next investigated the impact of scaffold flexibility. The original cube scaffold contains single-stranded 4 T segments at each corner to facilitate proper bending and folding (**Figure 1C**). These corners exhibit high flexibility as reflected by high RMSF (root mean square fluctuation) values in OxDNA simulations (**Figure S2C**).[47, 63, 64] To rigidify the scaffold, we introduced splint DNA strands diagonally across adjacent edges of the cube (**Figure 2I**). MD simulations revealed that the splinted cube would display increased rigidity, with the mean RMSF decreasing from 2.8 nm to 1.9 nm (**Figure S2E**). Hybridization of the DNA-6 T-peptide conjugates to the rigidified cube scaffold yielded clean assembly, as confirmed by native AGE

(**Figure 2K**, rDPCb). However, subsequent CD analysis of rDPCb showed a negative peak at 202 nm (**Figure S12A**, purple), consistent with a random coil conformation. Moreover, DLS measurements indicated a larger size and poorer dispersity compared to the corresponding DNA-only cube (**Figure S22B**). These results suggested that, on this rigid scaffold, the peptides fail to assemble properly within the cube interior (**Figure 2J**), likely because the structural rigidity prevents the intramolecular peptide "handshake" and constrains peptides in sub-optimal geometries that lack the dynamic flexibility needed for self-correction during assembly.

Taken together, these findings indicate that both linker length and scaffold flexibility are critical parameters for optimal scaffolded assembly. A linker of sufficient length is necessary to enable peptide-peptide interactions, while a certain degree of structural flexibility is required to accommodate conformational adjustments from the encapsulated peptides. Thus, the importance of the DNA scaffold does not just lie in increasing effective concentration of peptides. The geometry of the scaffold and of the linkers are essential in providing the correct orientation of the peptides for structural enzyme mimic properties.

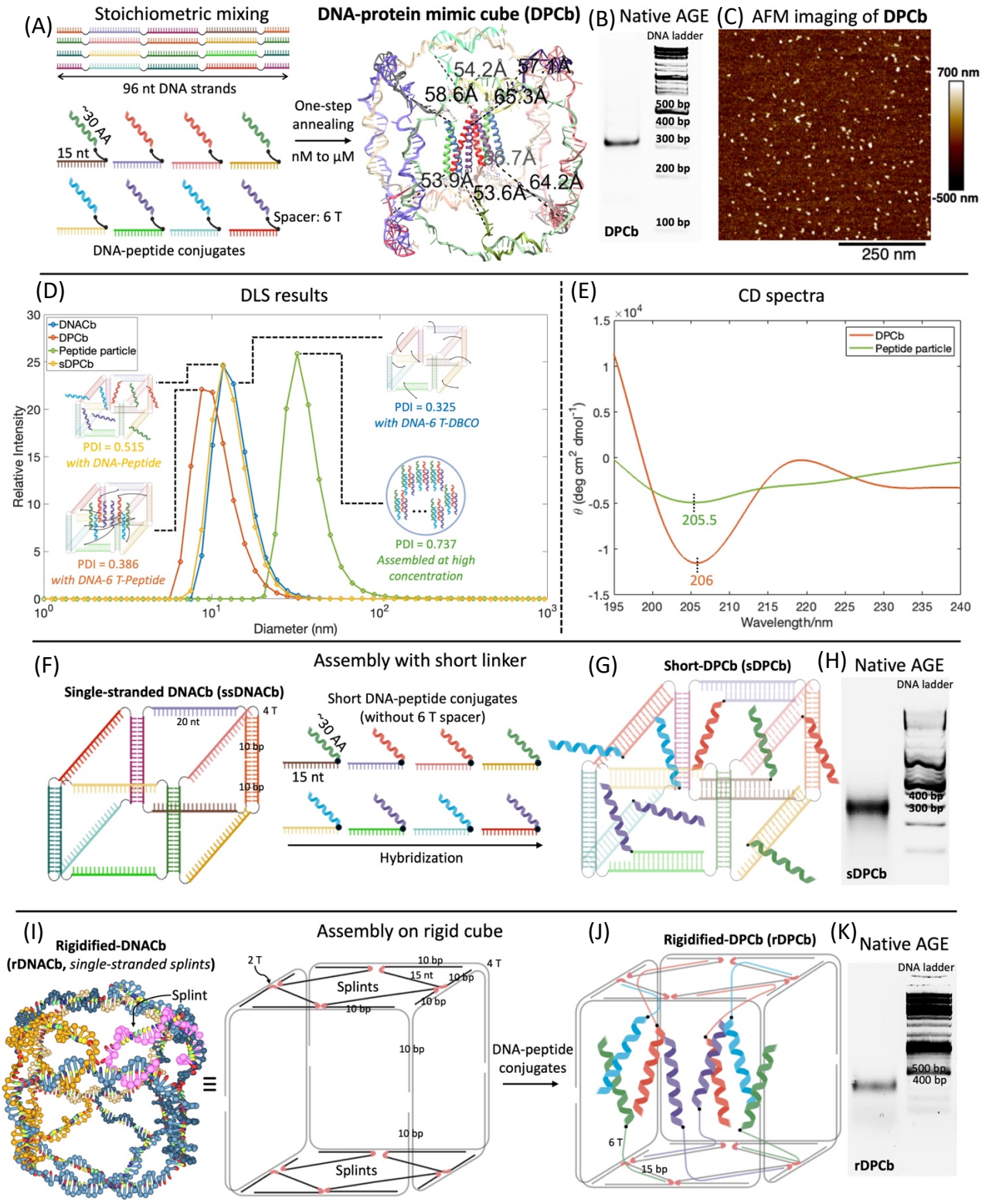


Figure 2. Optimization and assembly of cube scaffolded system. (A) One-step assembly of the DNA-protein mimic cube (DPCb) from linear strands. Distances between DNA and peptide are estimated and labelled. (B) 2% native AGE (agarose gel electrophoresis) showing the assembly of DPCb. GeneRuler DNA Ladder Mix was used in this study. (C) AFM imaging of DPCb. Discrete structures were observed. (D) DLS results of DPCb (with DNA-6 T-peptdie

conjugates), DNACb (with DNA-6 T-DBCO), peptide particles, and sDPCb (with DNA-peptide conjugates). DPCb, DNACb, and sDPCb were assembled at 1 μM structure concentration in 1xPBS buffer (**SI-VII**). Peptide particles were prepared by annealing 150 μM each of BF1-4 following the same procedures. Immediately prior to DLS measurements, the assembled peptide particles were diluted to a final concentration of 5 μM per peptide to achieve scattering intensities comparable to cube constructs. (E) CD spectra of DPCb and peptide particles. DPCb was measured at 1 μM structure concentration in 1xNaF buffer (**SI-I**) in the presence of 10 μM $FeSO_4$ (2.5 eq to the iron-binding sites). Peptides were measured at a final concentration of 150 μM each of BF1-BF4 in 1xNaF buffer with 0.75 mM $FeSO_4$ (2.5 eq to the iron binding sites). Detailed construct components are illustrated in **Table S3** and **Figure S5**. (F) Schematic representation of single-stranded DNA cube (ssDNACb). (G) Schematic representation of short DNA-peptide cube (sDPCb). (H) The assembly of sDPCb on 2% native AGE. (I) Left: the corresponding structural model generated in OxDNA with a splint strand highlighted; right: schematic representation of rigidified DNA cube (rDNACb) with single-stranded splint strands. More details are presented in **Figure S2**. (J) Schematic representation of rigidified DNA-peptide cube (rDPCb). (K) The assembly of rDPCb on 2% native AGE.

Ligand Binding of Protein Mimics

After confirming the assembly of DNA-protein mimic cube, we investigated its ligand binding properties. DPCb preserves iron binding residues within each subunit, in a similar manner to native Bfr (**Figure 3A**). The apo form of DPCb (without iron) exhibited a negative CD band at 203 nm (**Figure S13C**, blue), which transitioned to 206 nm upon addition of $FeSO_4$ (**Figure S13C**, orange). This shift indicates a conformational transition toward increased α-helical character upon iron binding. Upon oxidation of $FeSO_4$, DPCb also produced large aggregate-like features on AFM (**Figure 3D**). Native Bfr can oxidize Fe(II) to Fe(III) and stores the resulting mineral within its hollow cavity.[44, 66] Although the cube mimic lacks an internal storage cavity, it retains iron-binding sites and promotes iron oxidation as confirmed by UV-vis measurements (**SI-XI-2**). The observed aggregates are therefore possibly attributed to the formation of protein mimic-Fe(III) complexes.

To further validate the importance of metal-binding residues at the active site, we constructed a mutant cube for comparison. The modular assembly addresses each component strand individually, and peptide fragments can be readily exchanged without resynthesizing the entire polypeptide complex. Therefore, a variant lacking key metal-binding residues (**Figure 3B**) was assembled by modifying only two peptides (Glu to Leu, and His to Asn): BF2-M1 (E14L; H17N) and BF4-M1

(E14L; H17N). In the absence of these coordinating residues, DPCb-M1 exhibited a random coil signature by CD analysis in the presence of $FeSO_4$ (**Figure 3C**, orange), in contrast to the more ordered conformation of the original DPCb (**Figure 3C**, blue). This conformational change demonstrates the importance of metal-binding residues in stabilizing the assembled architecture. Functional differences were also observed by AFM. Unlike DPCb, the mutant construct showed no mineral-like aggregates after iron addition (**Figure 3E**), similar to that observed for the DNA-only cube (**Figure S9F**). These structural and functional differences support the iron-binding ability of the original mimic DPCb, and highlight the programmability of scaffolded assembly for probing sequence-function relationships in a modular way.

We next studied the heme binding properties of the mimic. In the original DPCb design, Met residues are positioned at the interface of subunits for heme binding (**Figure 3F**). UV-vis spectroscopy was used to assess this interaction by adding excess heme to the cubes to saturate the binding sites (heme:cube = 10:1 molar ratio). Compared to a control mixture of DNACb and free peptides (**Figure 3H**, yellow), DPCb exhibited increased absorbance in both the Soret and Q bands (**Figure 3H**, blue). This spectral difference indicates heme binding to the scaffolded protein mimic. Notably, the Soret maximum was positioned at ~400 nm when the cube was in excess (**Figure S16A**, left; heme:cube < 1) and shifted toward ~390 nm upon saturation with excess heme (**Figure S16B**, left; heme:cube > 1), likely owing to increased contribution from free heme in solution. The observed Soret features differ from the low-spin bis-methionine-coordinated heme of native Bfr (~418 nm), indicating that the scaffolded dimer interface does not perfectly mimic that of the native enzyme dimer. Achieving native-like axial ligation geometry represents a target for future peptide optimization. An independent titration experiment revealed a sub-micromolar K_D for DPCb (**Figure S15A&B**). Further evidence for heme binding was obtained through site-specific mutation

of the binding sites. We synthesized a mutant peptide BF2-M2, with Met replaced by non-coordinating Leu (**Figure 3G**). Although DPCb-M2 showed a well-defined assembly band on native AGE (**Figure S6F**), it did not display an increase in absorbance upon heme addition in UV-vis spectra (**Figure 3H**, orange). This indicates disruption of heme coordination in the absence of Met, and supports heme binding for the scaffolded mimic DPCb. Thermal denaturation experiments further revealed distinct behaviors among structures. The Soret band of heme is sensitive to its coordination environment and protein conformation and therefore serves as a probe for structural changes during unfolding. We monitored cubes containing equimolar amounts of heme by following the absorbance at 400 nm during heating (**Figure 3I**). Without DNA scaffolding (**Figure 3J**, yellow) or when the Met residue at the binding site was mutated (**Figure 3J**, orange), the heme-containing samples displayed increasing absorbance at 400 nm with increasing temperature. Given that hydrophobic heme molecule can aggregate in aqueous buffer which results in reduced absorbance,[67] this trend likely reflects changes in the aggregation state and solvent exposure of free heme. By contrast, DPCb-heme showed an overall decrease in absorbance upon heating (**Figure 3J**, blue), indicating disruption of the heme-peptide coordination environment. It is noted that signal fluctuations were observed between 50 to 60 °C. As these fluctuations occur within the temperature range of cube dissociation (**Figure S14C**) and after DNA melting (~45 °C, **Figure S14B**), we attribute them to transient peptide reorganization within partially dissociated structures. The overall decreasing trend reflects the loss of the original heme binding site throughout thermal denaturation. Collectively, these results support the proposed cube-protein mimic model and confirm its heme-binding capability. The modular DNA-scaffolded approach provides additional evidence for studying sequence-structure relationships, where the importance of Met in heme binding can be demonstrated through modification of a single component.

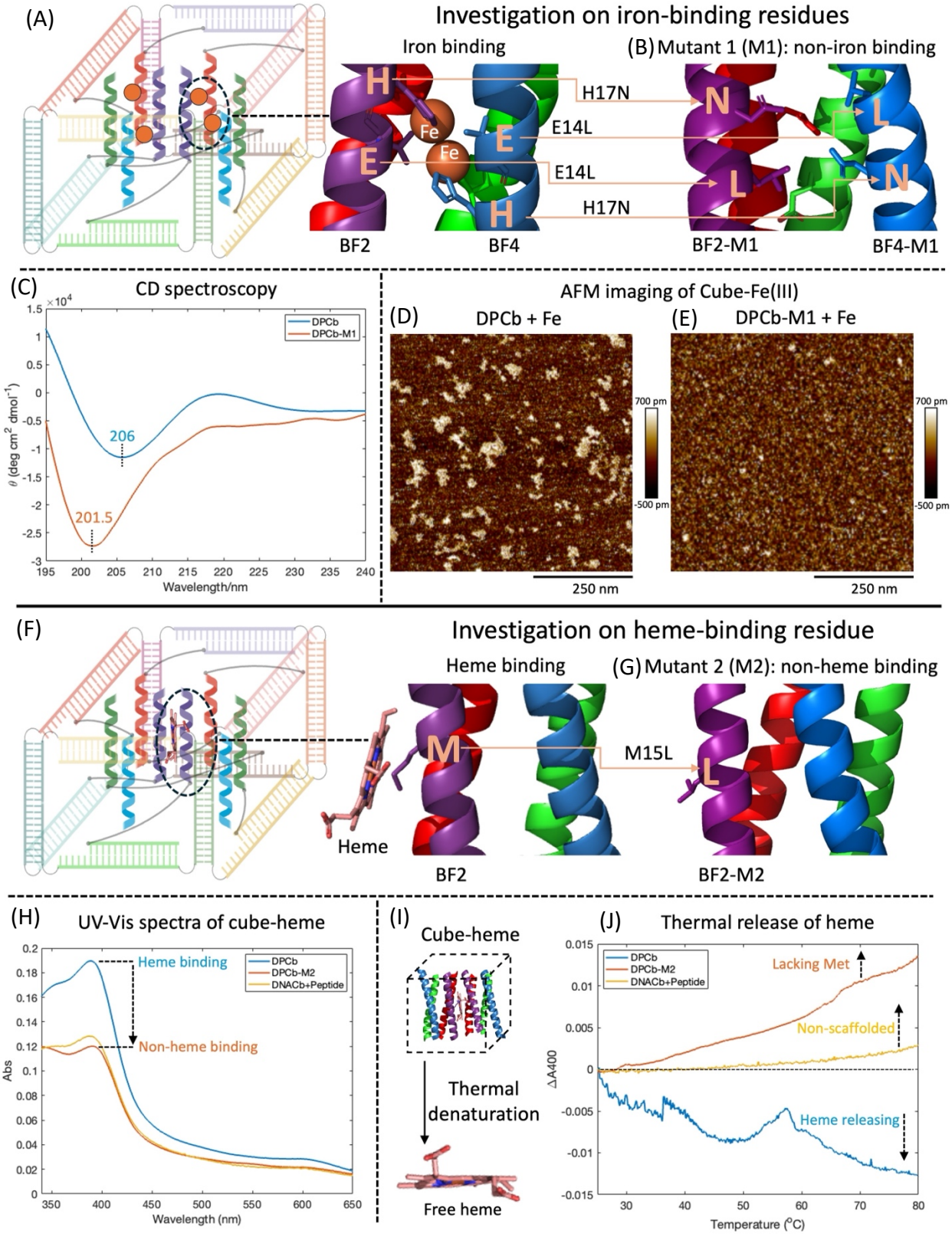


Figure 3. Sequence control of protein mimics by site-specific mutations. (A) Schematic representation of DPCb-Fe and zoomed-in view of the diiron site. In this study, peptide conformations shown in cartoon representation were

predicted using AlphaFold. More details are presented in **Figure S13**. (B) Zoomed-in view of the central site of DPCb-M1. (C) CD spectra of 1 μM DPCb and DPCb-M1 in 1xNaF buffer containing 10 μM $FeSO_4$. (D) AFM image of DPCb in the presence of Fe(III). (E) AFM image of DPCb-M1 in the presence of Fe(III). Experimental details and full-size AFM images are shown in **SI-VIII**. (F) Schematic representation of DPCb-heme and zoomed-in view of the heme site. (G) Zoomed-in view of DPCb-M2. (H) UV-vis spectra of cube-heme in 1xPBS buffer. Blue: 1 μM DPCb + 10 μM heme; orange: 1 μM DPCb-M2 + 10 μM heme; yellow: 1 μM DNACb + 2 μM each of peptides BF1-4 + 10 μM heme. (I) Schematic representation of heme releasing from the cube during thermal denaturation. (J) Abs-400 change with increasing temperature. Samples contained 1 μM cube in 1xPBS with equimolar heme.

Subunit Orientation Control within Cube Scaffold

In addition to generating architectures with variant sequences, the three-dimensional DNA cube serves as a programmable platform to modulate the spatial positioning and orientation of the same set of peptide subunits. In native Bfr, subunit arrangements are dictated by evolutionarily conserved assembly rules encoded at specific interfacial residues, which restricts how subunits associate in a defined set of permissible configurations.[68] Altering these orientations through protein-protein interactions alone can therefore be challenging. Instead, with structural support orthogonal to peptide motifs, the DNA scaffold facilitates more flexible control over subunit orientation. By simply swapping the connected DNA strands, peptides can be anchored to either the top or bottom rim of the cube, thereby modulating their orientation within the central cavity.

Using this approach, we assembled a DNA-protein mimic cube with a subunit arrangement distinct from the original DPCb featuring two parallel subunits (**Figure 4A**). In the new construct NDPCb, we positioned the two subunits in an antiparallel configuration (**Figure 4B**), resembling the arrangement observed in native Bfr. This structure assembled efficiently (**Figure S6E**) and exhibited a similar CD pattern at room temperature (**Figure S13E**, orange). In addition, UV-vis analysis (**Figure 4C**) showed that both cube constructs are capable of oxidizing Fe(II) to Fe(III), as evidenced by spectral changes in the iron mineral-associated region around 340 nm.[69] These results are consistent with the fact that iron binding and oxidation occur within individual

subunits.[44] In this study, DPCb and NDPCb encapsulate the same peptide subunits, differing only in their relative orientation within the cube scaffold. As such, processes localized within a single subunit are not expected to be strongly influenced by global subunit arrangement. In contrast, heme binding in native Bfr occurs at the interface between two adjacent subunits.[70] The relative orientation of neighboring subunits is therefore likely to have a more direct influence on heme binding behavior. This difference is supported by UV-vis spectroscopy. When the same concentration of each cube was mixed with the same amount of heme, the two constructs showed distinct Soret band intensities (**Figure S16A**). The spectral difference became more pronounced after the binding sites were saturated with excess heme (**Figure S16B**).

To further probe the structural differences of altered subunit orientation, we carried out thermal denaturation studies. CD melting experiments revealed different conformational transitions upon heating. In DPCb, the peptide motifs predominantly transitioned to random coil above 55 °C, with the negative peak position gradually shifting toward 200 nm (**Figure 4D**). In contrast, NDPCb exhibited an α-helix melting pattern throughout the heating process (**Figure 4E**). Subsequent UV-260 melting showed that both constructs have similar melting temperatures at around 58 °C (**Figure 4F**). However, NDPCb showed a more cooperative melting transition than DPCb, as indicated by an 11 °C narrower melting window (**Figure S14C**). These differences in thermal behavior suggest that subunit orientation affects peptide-peptide interactions at the interface and leads to different melting pathways, which would be otherwise difficult to study without DNA scaffolding.

Cryo-electron Microscopy Characterization

To validate the structural integrity of the constructs, we visualized three representative samples by cryo-EM: (A) DNACb, with flexible spacers but no peptides; (B) DPCb, with flexible spacers and

peptides but without iron or heme added; and (C) NDPCb with flexible spacers and peptides but in the presence of $FeSO_4$ and ferroheme (**Table S5**). Particle picking and 2D classification showed that all samples were heterogeneous, probably due to the intrinsic flexibility of the structures. For all samples, the 2D class averages included a mixture of shapes representing projections of distorted cubes (**Figure 4G-I** and **Figure S20**). Interestingly, several 2D class averages for the NDPCb sample showed internal densities within the cubic structure (**Figure 4H**). This internal density was not visible in any of the 2D class averages for the DNACb hollow or DPCb (peptides without Fe or heme) samples (**Figure S20**), indicating that the NPDCb assembly in the presence of iron and heme stabilized and rigidified the peptide bundle. We then attempted the reconstruction of NPDCb as this was the only sample displaying an internal density. As anticipated from the sample heterogeneity and cube dynamics, the flexibility of the structure precluded us from obtaining a high-resolution structure, in which all the DNA edges and the internal helical bundle were well defined. Nonetheless, we could generate a low-resolution 3D reconstruction showing well-defined density for one corner of the cube and its adjacent edges (**Figure 4I** and **Figure S21A-C**). The 3D reconstruction confirmed the presence of a density in the center of the structure, which we interpreted as the peptide helical bundle (**Figure 4I**). However, the limited resolution and features of these 3D map precluded us from building a full molecular model. We then performed a 3D variability analysis and confirmed the flexibility of the NDPCb assembly (**Figure S21D**). Importantly, the internal residual density was present in all the 3D classes from the variability analysis, confirming that the ligands stabilized the helical bundle. These results and the spectroscopic data validate the proposed DNA scaffold mimic structure.

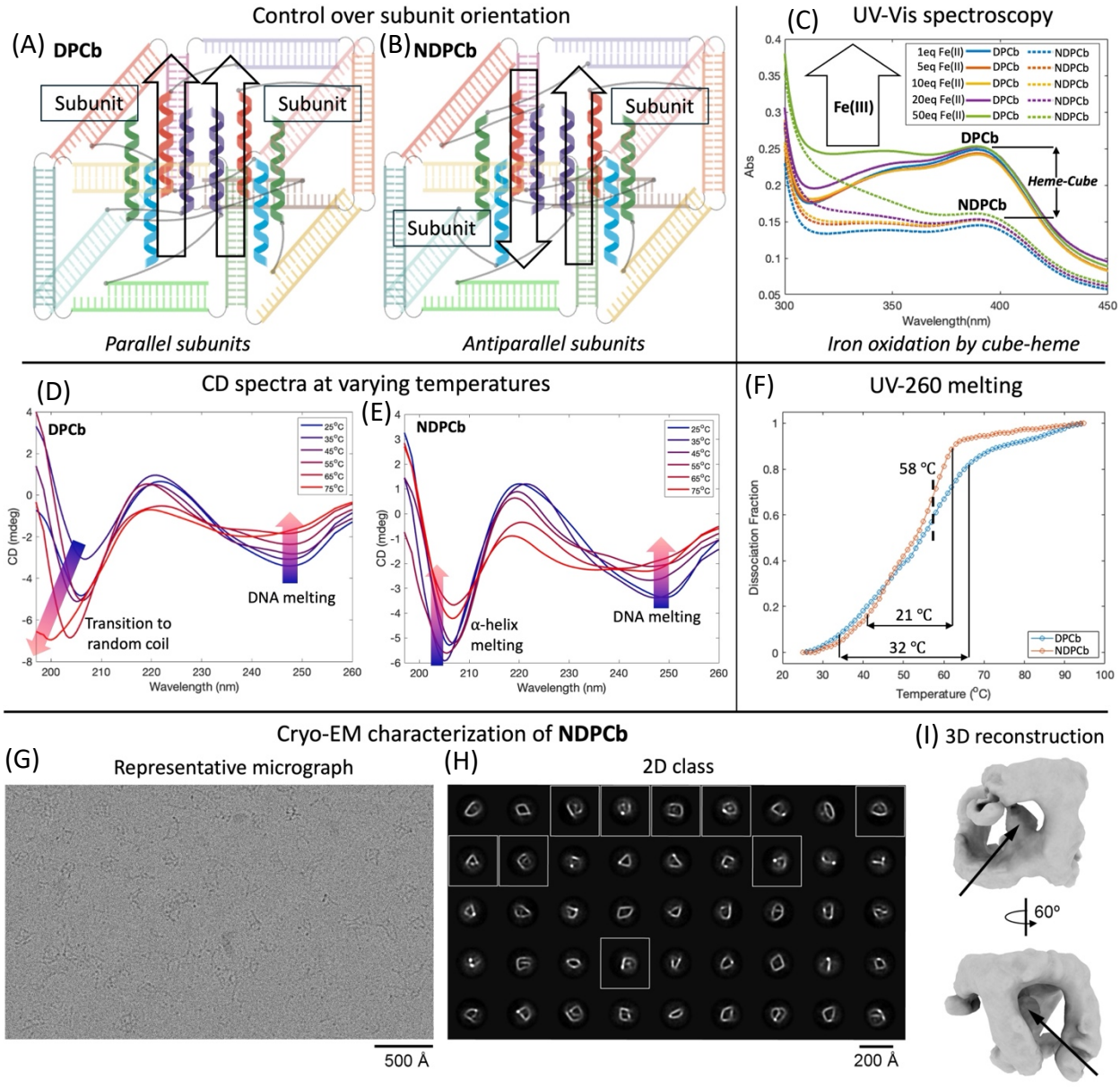


Figure 4. Subunit orientation control within cube scaffold. (A) Schematic representation of DPCb featuring two parallel subunits. (B) Schematic representation of NDPCb featuring two antiparallel subunits. (C) UV-vis spectra monitoring iron oxidation by DPCb (solid lines) and NDPCb (dotted lines) in the presence of heme. Increasing amount of $FeSO_4$ were added to 1 μM cube containing 10 μM ferroheme. Spectra were recorded after 10 minutes of aerobic incubation at room temperature to allow oxidation. Additional heme binding results are presented in **SI-XI-1**. (D) CD spectra of 1 μM DPCb at varying temperatures. (E) CD spectra of 1 μM NDPCb at varying temperatures. (F) UV-260 melting curves of DPCb (blue) and NDPCb (orange). Additional melting results are presented in **SI-X**. (G) Representative cryo-EM micrograph of NDPCb assembled in the presence of $FeSO_4$ and ferroheme. (H) 2D class averages of NDPCb. Gray squares highlight 2D classes with internal densities, consistent with ligand-stabilized peptide organization. (I) Two views of the 3D reconstruction of NDPCb with the internal density indicated with an arrow. Additional cryo-EM results are presented in **SI-XIII**.

Dynamic Regulation of Functionality

The design of protein structures with dynamic properties has been explored,[71-73] yet it remains challenging and often requires substantial computational effort. On the other hand, DNA nanotechnology has extensively demonstrated dynamic control over structure and function.[74-76] Its bottom-up assembly strategy makes each component individually addressable, resulting in modular generation of structural variants for systematic investigation of structure-function relationships. In this study, each cube edge contains a 5-nt unhybridized region, serving as structural handles for dynamic regulation by strand displacement (**Figure 5A**). Because each edge can be individually addressed, introducing fully complementary DNA strands at room temperature enables selective "erasing" of peptide components within the cube one-by-one (**Figure 5B**), and may allow fine-tuning of the catalytic activity. To demonstrate this, we employed a semiquinone radical assay, a reaction with moderate kinetics. It has been reported that the four-helix peptide bundle can promote semiquinone radical formation in a reversible manner by stabilizing the radical species through incorporated Zn(II) ions (**Figure 5C**).[77] Since the reactant 3,5-Di-tert-butyl-1,2-benzoquinone (Q) has an absorbance peak at 415 nm, changes in A415 signal intensity reflect reaction progress. We first assembled DPCb consisting of eight DNA-peptide conjugates (Cb-8DP) and added zinc ions, followed by the addition of a mixture of Q and 3,5-di-tert-butylcatechol (QH_2). The reaction proceeds reversibly, with a forward rate (r1) representing the conversion of Q and QH_2 into the 3,5-di-tert-butyl-semiquinone radical anion $SQ^{\bullet-}$, and a reverse rate (r2) for the reversion of $SQ^{\bullet-}$ back to the original substrates. Initially, a sharp decrease in A415 (**Figure 5D**, blue, r1>r2) was observed, which indicates substrate conversion to product $SQ^{\bullet-}$. To regulate this activity, we introduced displacing strands to progressively release peptide units from the cube. Displacing a single peptide led to a slower decrease in A415, reflecting reduced substrate

conversion (**Figure 5D**, yellow). As more peptides were released, the reaction rate continued to decline until a dynamic equilibrium was reached (**Figure 5D**, purple & green, r1≈r2). When only one or no peptide remained in the cube, the A415 signal began to increase, which indicates substrate regeneration driven by the reverse reaction (**Figure 5D**, cyan & red, r1<r2). A concurrent change in A740 associated with the radical product was also detected (**Figure S19D**). In addition, DPCb-M1 lacking metal binding residues showed no activity with the reactants Q/QH_2 (**Figure S19B**). These results provide additional evidence to confirm the reaction process and dynamics.

To further validate this regulation, we performed the semiquinone assay on cubes with increasing number of peptides. Cube structures containing varying peptide numbers were first prepared via strand displacement (**Figure 5B)**, followed by addition of the QH_2/Q substrate mixture. Kinetic analysis of A415 revealed a range of substrate conversion rates (**Figure 5E**). Cubes with fewer than three encapsulated peptides failed to promote $SQ^{\bullet-}$ formation, whereas structures with more than four peptides exhibited increasing reaction rates as additional peptides were incorporated. This suggests that a more packed cube cavity enhances substrate conversion. It is noted that the substrate consumption rate in cube with two subunits was nearly double that of the cube containing only one subunit, supporting the reliability of this methodology. Overall, these findings demonstrate that DNA scaffolding provides an effective allosteric approach to control, switch catalytic performance, as well as to tune it to specific values through strand displacement, enabling dynamic and tunable enzymatic activity.

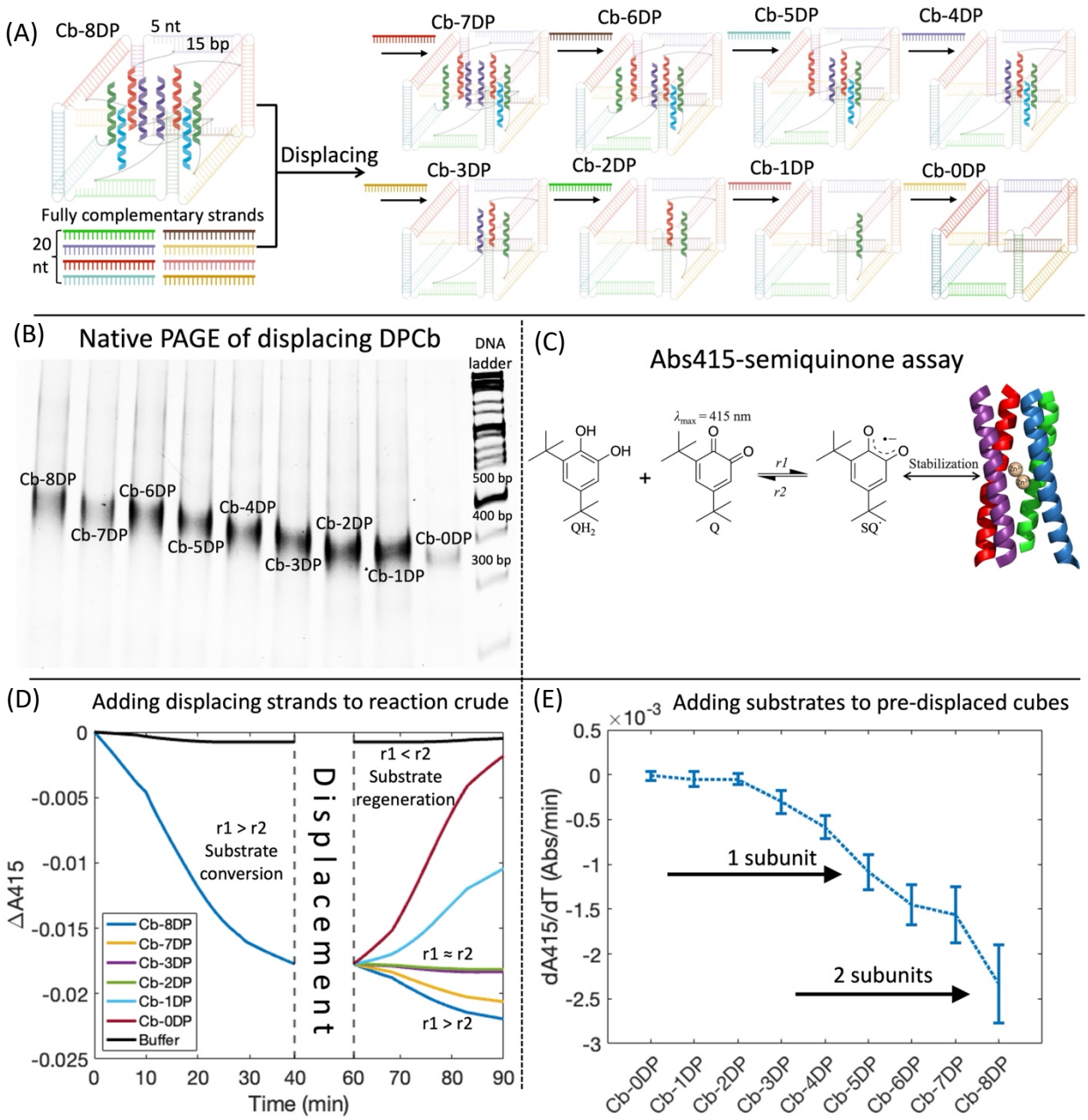


Figure 5. Dynamic control over functionality by strand displacement. (A) Schematic representation of strand displacement on DPCb consisting of eight DNA-peptide conjugates (Cb-8DP). (B) A 5% native polyacrylamide gel electrophoresis (PAGE) showing the cube structures with different numbers of peptides by strand displacement. GeneRuler DNA Ladder Mix was employed. (C) Overview of the semiquinone assay. The transient $SQ^{\bullet}$ can be stabilized by zinc-polypeptide. (D) Dynamic control of the reaction progress by DNA strand displacement. The equilibrium change was shown by UV-vis kinetics at 415 nm. $ZnSO_4$ (2.5 eq to metal binding site) solution was added to pre-assembled DPCb. This solution was then incubated with a mixture of the substrates QH_2/Q for 40 minutes. Afterwards, varying numbers of fully complementary DNA strands were introduced and incubated for 20 minutes at room temperature for equilibration. The A415 kinetic reading was resumed at the 60th minute. (E) Substrate conversion rates represented by $\Delta A415/\Delta t$ versus the number of peptides per cube. The values were calculated based on the first 10 minutes of reaction, where $\Delta A415$ is proportional to Δt. Each point comprises three individual measurements. Additional results were presented in **Figure S19**.

Assembly of Bacterioferritin Capsule Mimic

Proteins can assemble into higher order complexes that yield nanostructures with new geometries and distinct functional properties.[3, 23, 78, 79] However, the formation of these structures is governed by a complex array of interactions, including hydrophobic effect, hydrogen bonding , electrostatic interactions and conformational dynamics. These interactions are tightly coupled to folding pathways encoded in the protein sequences. Consequently, the design and production of new higher-order protein assemblies remain non-trivial and often require iterative computational and experimental optimization. In contrast, DNA-based assembly offers a simple, predictable, and efficient strategy for constructing higher order architectures.[80] DNA scaffolds assemble through sequence specific Watson-Crick-Franklin base pairing, which strongly favors predesigned strand hybridization over nonspecific interactions. This strategy can operate orthogonally to protein interactions and offer precise control over the spatial arrangement of attached payloads with high assembly fidelity.[81-83]

The previously described cube consists of two peptide subunits per structure. In principle, organizing multiple cubes into a larger complex would increase the number of subunits presented on the exterior, leading to a topology that more closely resembles native Bfr. To explore the potential of assembling encapsulated protein mimics into higher-order structures, we used a spherical nucleic acid (SNA) scaffold previously developed by our group (**Figure 6A**).[84] SNA is a nanosphere with nucleic acids exposed on its corona and hydrophobic polymers in its core, allowing for facile functionalization via DNA hybridization (Lane 1: SNA, **Figure 6B**). To enable assembly, we designed a DPCb variant, featuring four DNA overhang strands complementary to the SNA sequence. This overhang cube-peptide construct assembled well, with a single band on

AGE (Lane 2: DPCb-Overhang, **Figure 6B**). Owing to the rapid and reliable nature of DNA hybridization, higher order protein mimic assemblies formed readily upon simple mixing of preassembled DPCb-Overhang with SNA at room temperature, as indicated by a clear AGE band (Lane 3: DPCb-SNA, **Figure 6B**). We confirmed the fidelity of this assembly by DLS analysis. As shown in **Figure 6C**, the size of DPCb-SNA closely matched the theoretical sum of DPCb-Overhang and SNA, and the assembled structure exhibited an improved monodispersity (PDI = 0.3, **Figure 6C**). AFM further characterized the assembly. A 4.4-fold excess of cube structures, with and without complementary overhangs, were preassembled and mixed with SNA. In the absence of overhang strands, no cooperative structures were observed; AFM imaging shows the SNA (higher structures) and the cube as separate structures (smaller, lower height structures, **Figure 6D**). However, when overhangs are present, cube-protein mimics were seen attached to the SNA surface, with free cubes disappearing from the background (**Figure 6E**). This comparison indicates that the assembly is directed by DNA hybridization rather than nonspecific interactions. Notably, cubes mixed at different ratios relative to SNA (**Figure S7** & **S22C**), and cubes bearing different subunit orientations (NDPCb, **Figure S8**) also formed higher-order complexes using this strategy. This one-step assembly method enables protein mimics to organize into higher order architectures and underscores the precision and versatility of the DNA scaffolding approach. The resulting Bfr capsule-mimic adopts a similar topology to its natural counterpart, with subunits arranged around a central micelle (albeit with a hydrophobic core, instead of a hollow cavity). The increased number of subunits presented within each assembly promotes a higher local density of active sites, which may accelerate the dynamics of iron transport in and out of the catalytic centers. As a result, the complex exhibits enhanced iron oxidation activity, with a kinetic constant (k_{fast}) approximately twofold higher than that of individual cubes at the same total subunit concentration

(**Figure S17**). The increased subunit local concentration represents the most prominent structural distinction between the higher-order complexes and individual cubes, and is therefore a likely contributor to the enhanced activity. Additional contributions may arise from changes in the local microenvironment at the micelle core or subunit interface. It is worth noting that the core chemistry of the SNA micelle can be readily tuned via solid-phase synthesis.[85-87] By adjusting the hydrophobic block composition and sequence, chain length, steric bulk, or incorporating residues with specific biochemical properties, the micellar complex can be further optimized or customized to diverse applications. The simplicity and modularity of assembling higher-order complexes further highlight the potential of this platform for constructing hierarchically organized and scalable assemblies.

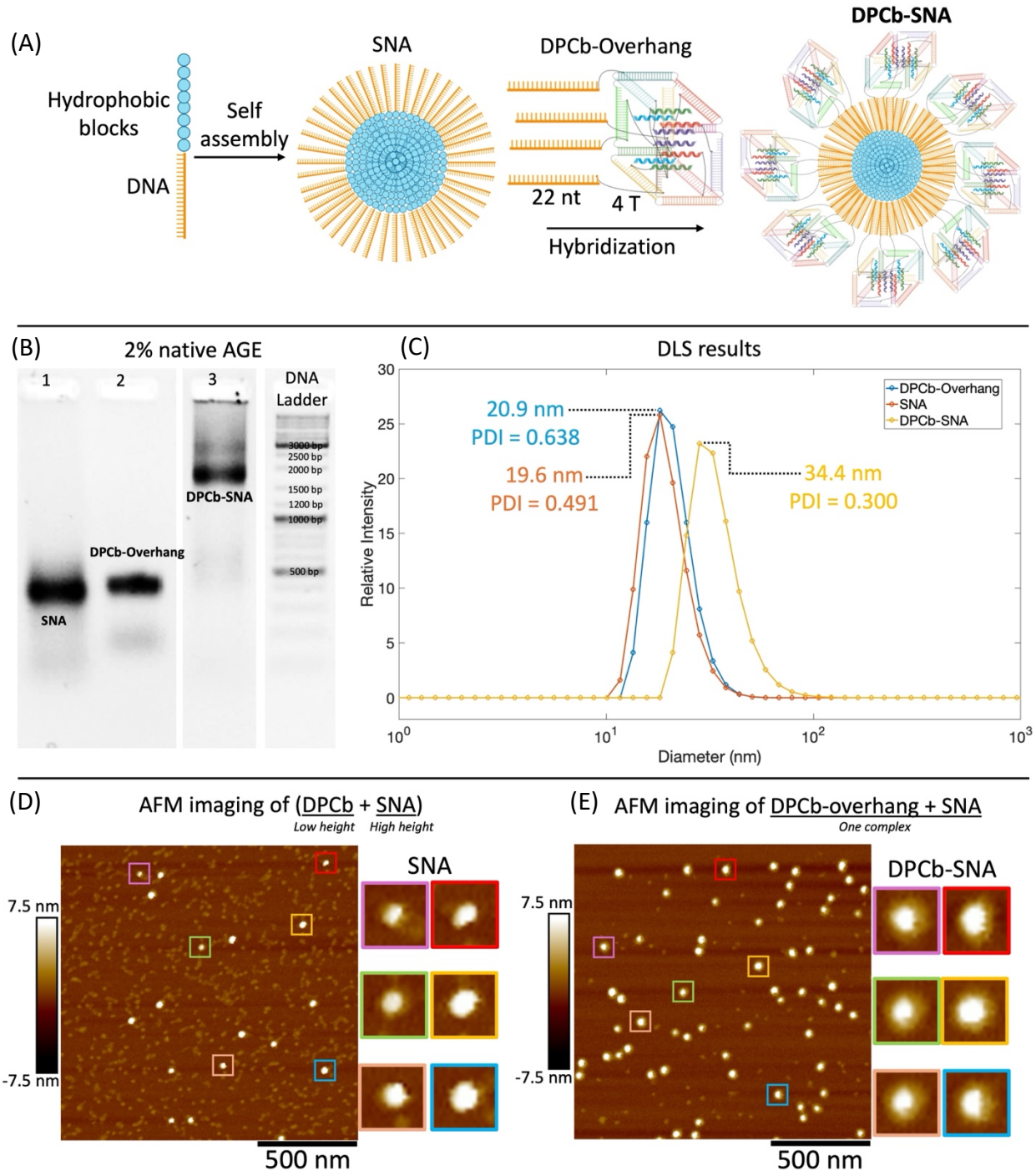


Figure 6. Assembly of mimic of the bacterioferritin capsule. (A) Schematic representation of the assembly approach. Featuring complementary overhangs, cube-protein mimic can spontaneously assemble with a SNA into higher-order complexes. (B) A 2% native agarose gel electrophoresis (AGE) showing the assembly of DPCb-SNA. GeneRuler DNA Ladder Mix was employed. Full size gel image can be found in **Figure S7**. (C) DLS results of DPCb-Overhang (blue), SNA (orange) and DPCb-SNA (yellow). Additional DLS results were provided in **Figure S22C**. (D) AFM imaging of the mixture of DPCb and SNA. Separate structures were observed without cube overhangs. (E) AFM imaging of DPCb-SNA. Higher-order complexes were revealed when the cube features complementary overhangs.

Conclusion

We have developed a versatile and programmable method to construct functional protein mimics by DNA scaffolding. This approach offers full control over sequence composition, spatial arrangement of subunit directionality, and conformational regulation of the encapsulated protein mimics. It enables the systematic exploration of sequence-structure-function relationships. Structures with different subunit orientations were obtained via this modular assembly method, allowing for exploration into the impact of subunit interface on the structural stability and functionality. A key advantage of this method is its ability to bypass the complex protein folding process, revealing underlying folding principles that are otherwise hidden in alternative protein engineering methods. The concept of template-assembled synthetic proteins (TASPs) has been advanced earlier.[88] However, creating complex templates with different orthogonal reactivities on each peptide binding arm is synthetically challenging, and this synthetic complexity increases with the number of different peptides. This is likely the reason that this approach has not yet made a large impact on protein mimicry. DNA nanostructures, on the other hand, provide highly modular and programmable templates to position different peptides in nearly infinite geometries and arrangements. It is now straightforward to obtain DNA strands from commercial providers, including functionalized strands for conjugation, that can be readily assembled into a multitude of nanostructures and conjugated with peptides. These can be used as highly programmable templates that make the TASPs approach easily to achieve and the diversity of templates highly accessible.

The DNA scaffold not only increases effective concentration of peptides to promote assembly, but also plays a critical role in defining their spatial orientation and interactions. By programming the scaffold components, structural variants of the cube can be generated modularly and result in distinct structural and functional properties. These changes underscore the importance of scaffold

geometry in directing optimal assembly and function. This level of control provides unique insights into structural and functional regulation. For example, it revealed that the subunit arrangement results in different heme binding and thermal melting pathways. The extracted design principles can be further applied to engineer proteins with tailored functionalities, expanding the potential of protein design. By creating an independently stable active site, we can now treat the active site like a synthetic organometallic catalyst and optimize function without distorting the peptide arrangement.

Beyond the structural advantages, our DNA-scaffolded protein mimic system exhibits diverse functional capabilities, including heme binding, iron oxidation, and semiquinone radical stabilization. Moreover, catalytic activity can be precisely tuned and switched on and off using dynamic DNA strand displacement, demonstrating exceptional control over enzyme-mimicking processes. By merging the addressability of DNA nanotechnology with the functional diversity of peptide motifs, this strategy provides a powerful platform for biomolecular engineering. The programmability of DNA hybridization additionally allows for the construction of higher-order assemblies, such as a bacterioferritin capsule mimic formed by hybridizing DNA cubes with spherical nucleic acids. This modular design principle is highly generalizable and can be extrapolated to other protein systems, making it a valuable tool for future protein engineering and synthetic biology research.

Looking ahead, we envision expanding this method to construct barcoded protein mimic libraries, which will enable high-throughput screening of novel protein structures and catalytic functionalities, and will accelerate discoveries in protein folding, enzymatic catalysis, and biomolecular design. By integrating DNA nanotechnology with protein engineering, this approach

holds significant promise for the rational design of novel protein motifs with precisely regulated structural and functional properties.

Reference

(1) Pan, X.; Kortemme, T. Recent advances in de novo protein design: Principles, methods, and applications. *Journal of Biological Chemistry* **2021**, *296*, 100558. DOI: https://doi.org/10.1016/j.jbc.2021.100558.
(2) Huang, P.-S.; Boyken, S. E.; Baker, D. The coming of age of de novo protein design. *Nature* **2016**, *537* (7620), 320-327. DOI: 10.1038/nature19946.
(3) Huddy, T. F.; Hsia, Y.; Kibler, R. D.; Xu, J.; Bethel, N.; Nagarajan, D.; Redler, R.; Leung, P. J. Y.; Weidle, C.; Courbet, A.; et al. Blueprinting extendable nanomaterials with standardized protein blocks. *Nature* **2024**, *627* (8005), 898-904. DOI: 10.1038/s41586-024-07188-4.
(4) Bermeo, S.; Favor, A.; Chang, Y.-T.; Norris, A.; Boyken, S. E.; Hsia, Y.; Haddox, H. K.; Xu, C.; Brunette, T. J.; Wysocki, V. H.; et al. De novo design of obligate ABC-type heterotrimeric proteins. *Nature Structural & Molecular Biology* **2022**, *29* (12), 1266-1276. DOI: 10.1038/s41594-022-00879-4.
(5) Abramson, J.; Adler, J.; Dunger, J.; Evans, R.; Green, T.; Pritzel, A.; Ronneberger, O.; Willmore, L.; Ballard, A. J.; Bambrick, J.; et al. Accurate structure prediction of biomolecular interactions with AlphaFold 3. *Nature* **2024**, *630* (8016), 493-500. DOI: 10.1038/s41586-024-07487-w.
(6) Watson, J. L.; Juergens, D.; Bennett, N. R.; Trippe, B. L.; Yim, J.; Eisenach, H. E.; Ahern, W.; Borst, A. J.; Ragotte, R. J.; Milles, L. F.; et al. De novo design of protein structure and function with RFdiffusion. *Nature* **2023**, *620* (7976), 1089-1100. DOI: 10.1038/s41586-023-06415-8.
(7) Ahern, W.; Yim, J.; Tischer, D.; Salike, S.; Woodbury, S. M.; Kim, D.; Kalvet, I.; Kipnis, Y.; Coventry, B.; Altae-Tran, H. R.; et al. Atom-level enzyme active site scaffolding using RFdiffusion2. *Nature Methods* **2025**. DOI: 10.1038/s41592-025-02975-x.
(8) Kim, D.; Woodbury, S. M.; Ahern, W.; Tischer, D.; Kang, A.; Joyce, E.; Bera, A. K.; Hanikel, N.; Salike, S.; Krishna, R.; et al. Computational design of metallohydrolases. *Nature* **2025**. DOI: 10.1038/s41586-025-09746-w.
(9) Terwilliger, T. C.; Liebschner, D.; Croll, T. I.; Williams, C. J.; McCoy, A. J.; Poon, B. K.; Afonine, P. V.; Oeffner, R. D.; Richardson, J. S.; Read, R. J.; et al. AlphaFold predictions are valuable hypotheses and accelerate but do not replace experimental structure determination. *Nature Methods* **2024**, *21* (1), 110-116. DOI: 10.1038/s41592-023-02087-4.
(10) Agarwal, V.; McShan, A. C. The power and pitfalls of AlphaFold2 for structure prediction beyond rigid globular proteins. *Nature Chemical Biology* **2024**, *20* (8), 950-959. DOI: 10.1038/s41589-024-01638-w.
(11) Wang, J.; Lisanza, S.; Juergens, D.; Tischer, D.; Watson, J. L.; Castro, K. M.; Ragotte, R.; Saragovi, A.; Milles, L. F.; Baek, M.; et al. Scaffolding protein functional sites using deep learning. *Science* **2022**, *377* (6604), 387-394. DOI: doi:10.1126/science.abn2100.
(12) Chu, A. E.; Lu, T.; Huang, P.-S. Sparks of function by de novo protein design. *Nature Biotechnology* **2024**, *42* (2), 203-215. DOI: 10.1038/s41587-024-02133-2.
(13) Mutter, M.; Vuilleumier, S. A Chemical Approach to Protein Design—Template-Assembled Synthetic Proteins (TASP). *Angew. Chem., Int. Ed. Engl.* **1989**, *28* (5), 535-554. DOI: https://doi.org/10.1002/anie.198905353.
(14) Wong, A. K.; Jacobsen, M. P.; Winzor, D. J.; Fairlie, D. P. Template Assembled Synthetic Proteins (TASPs). Are Template Size, Shape, and Directionality Important in Formation of Four-Helix Bundles? *J. Am. Chem. Soc.* **1998**, *120* (16), 3836-3841. DOI: 10.1021/ja971951o.
(15) Freeman, J. O.; Lee, W. C.; Murphy, M. E. P.; Sherman, J. C. X-ray Crystal Analysis of a TASP: Structural Insights of a Cavitein Dimer. *J. Am. Chem. Soc.* **2009**, *131* (21), 7421-7429. DOI: 10.1021/ja901404w.
(16) Wuo, M. G.; Mahon, A. B.; Arora, P. S. An Effective Strategy for Stabilizing Minimal Coiled Coil Mimetics. *J. Am. Chem. Soc.* **2015**, *137* (36), 11618-11621. DOI: 10.1021/jacs.5b05525.
(17) Wuo, M. G.; Hong, S. H.; Singh, A.; Arora, P. S. Synthetic Control of Tertiary Helical Structures in Short Peptides. *J. Am. Chem. Soc.* **2018**, *140* (47), 16284-16290. DOI: 10.1021/jacs.8b10082.
(18) Dang, B.; Wu, H.; Mulligan, V. K.; Mravic, M.; Wu, Y.; Lemmin, T.; Ford, A.; Silva, D.-A.; Baker, D.; DeGrado, W. F. De novo design of covalently constrained mesosize protein scaffolds with unique tertiary structures. *Proc. Natl Acad. Sci.* **2017**, *114* (41), 10852-10857. DOI: doi:10.1073/pnas.1710695114.
(19) Song, W. J.; Yu, J.; Tezcan, F. A. Importance of Scaffold Flexibility/Rigidity in the Design and Directed Evolution of Artificial Metallo-β-lactamases. *J. Am. Chem. Soc.* **2017**, *139* (46), 16772-16779. DOI: 10.1021/jacs.7b08981.
(20) Lombardi, A.; Pirro, F.; Maglio, O.; Chino, M.; DeGrado, W. F. De Novo Design of Four-Helix Bundle Metalloproteins: One Scaffold, Diverse Reactivities. *Acc. Chem. Res.* **2019**, *52* (5), 1148-1159. DOI: 10.1021/acs.accounts.8b00674.
(21) Hoffnagle, A. M.; Tezcan, F. A. Atomically Accurate Design of Metalloproteins with Predefined Coordination Geometries. *J. Am. Chem. Soc.* **2023**, *145* (26), 14208-14214. DOI: 10.1021/jacs.3c04047.

(22) Aupič, J.; Strmšek, Ž.; Lapenta, F.; Pahovnik, D.; Pisanski, T.; Drobnak, I.; Ljubetič, A.; Jerala, R. Designed folding pathway of modular coiled-coil-based proteins. *Nat. Commun.* **2021**, *12* (1), 940. DOI: 10.1038/s41467-021-21185-5.
(23) Zhu, J.; Avakyan, N.; Kakkis, A.; Hoffnagle, A. M.; Han, K.; Li, Y.; Zhang, Z.; Choi, T. S.; Na, Y.; Yu, C.-J.; et al. Protein Assembly by Design. *Chem. Rev.* **2021**, *121* (22), 13701-13796. DOI: 10.1021/acs.chemrev.1c00308.
(24) Tolbert, A. E.; Ervin, C. S.; Ruckthong, L.; Paul, T. J.; Jayasinghe-Arachchige, V. M.; Neupane, K. P.; Stuckey, J. A.; Prabhakar, R.; Pecoraro, V. L. Heteromeric three-stranded coiled coils designed using a Pb(ii)(Cys)3 template mediated strategy. *Nat. Chem.* **2020**, *12* (4), 405-411. DOI: 10.1038/s41557-020-0423-6.
(25) Burton, A. J.; Thomson, A. R.; Dawson, W. M.; Brady, R. L.; Woolfson, D. N. Installing hydrolytic activity into a completely de novo protein framework. *Nat. Chem.* **2016**, *8* (9), 837-844. DOI: 10.1038/nchem.2555.
(26) Barber, B. E.; Jamieson, E. M. G.; White, L. E. M.; McTernan, C. T. Embracing Complexity: Peptides as Tunable Scaffolds in the Construction of Discrete Supramolecular Systems. *Angew. Chem. Int. Ed.* **2025**, *64* (34), e202512014. DOI: https://doi.org/10.1002/anie.202512014.
(27) Laporte, A. A. H.; Reek, J. N. H. Supramolecular Materials and Strategies for Bioorthogonal Chemical Transformations. *Chem. Rev.* **2025**, *125* (15), 7223-7274. DOI: 10.1021/acs.chemrev.5c00047.
(28) Beal, D. M.; Jones, L. H. Molecular Scaffolds Using Multiple Orthogonal Conjugations: Applications in Chemical Biology and Drug Discovery. *Angew. Chem. Int. Ed.* **2012**, *51* (26), 6320-6326. DOI: https://doi.org/10.1002/anie.201200002.
(29) Müller, C.; Despras, G.; Lindhorst, T. K. Organizing multivalency in carbohydrate recognition. *Chemical Society Reviews* **2016**, *45* (11), 3275-3302, 10.1039/C6CS00165C. DOI: 10.1039/C6CS00165C.
(30) Brabez, N.; Lynch, R. M.; Xu, L.; Gillies, R. J.; Chassaing, G.; Lavielle, S.; Hruby, V. J. Design, Synthesis, and Biological Studies of Efficient Multivalent Melanotropin Ligands: Tools toward Melanoma Diagnosis and Treatment. *Journal of Medicinal Chemistry* **2011**, *54* (20), 7375-7384. DOI: 10.1021/jm2009937.
(31) Goverde, C. A.; Pacesa, M.; Goldbach, N.; Dornfeld, L. J.; Balbi, P. E. M.; Georgeon, S.; Rosset, S.; Kapoor, S.; Choudhury, J.; Dauparas, J.; et al. Computational design of soluble and functional membrane protein analogues. *Nature* **2024**, *631* (8020), 449-458. DOI: 10.1038/s41586-024-07601-y.
(32) Marcos, E.; Chidyausiku, T. M.; McShan, A. C.; Evangelidis, T.; Nerli, S.; Carter, L.; Nivón, L. G.; Davis, A.; Oberdorfer, G.; Tripsianes, K.; et al. De novo design of a non-local β-sheet protein with high stability and accuracy. *Nature Structural & Molecular Biology* **2018**, *25* (11), 1028-1034. DOI: 10.1038/s41594-018-0141-6.
(33) Korbeld, K. T.; Viliuga, V.; Fürst, M. Limitations of the refolding pipeline for *de novo* protein design. *bioRxiv* **2025**, 2025.2012.2009.693122. DOI: 10.64898/2025.12.09.693122.
(34) Dauparas, J.; Anishchenko, I.; Bennett, N.; Bai, H.; Ragotte, R. J.; Milles, L. F.; Wicky, B. I. M.; Courbet, A.; de Haas, R. J.; Bethel, N.; et al. Robust deep learning–based protein sequence design using ProteinMPNN. *Science* **2022**, *378* (6615), 49-56. DOI: doi:10.1126/science.add2187.
(35) Pacesa, M.; Nickel, L.; Schellhaas, C.; Schmidt, J.; Pyatova, E.; Kissling, L.; Barendse, P.; Choudhury, J.; Kapoor, S.; Alcaraz-Serna, A.; et al. One-shot design of functional protein binders with BindCraft. *Nature* **2025**. DOI: 10.1038/s41586-025-09429-6.
(36) Lou, C.; Martos-Maldonado, M. C.; Madsen, C. S.; Thomsen, R. P.; Midtgaard, S. R.; Christensen, N. J.; Kjems, J.; Thulstrup, P. W.; Wengel, J.; Jensen, K. J. Peptide-oligonucleotide conjugates as nanoscale building blocks for assembly of an artificial three-helix protein mimic. *Nat Commun* **2016**, *7*, 12294. DOI: 10.1038/ncomms12294 From NLM.
(37) Lou, C.; Boesen, J. T.; Christensen, N. J.; Sørensen, K. K.; Thulstrup, P. W.; Pedersen, M. N.; Giralt, E.; Jensen, K. J.; Wengel, J. Self-Assembly of DNA–Peptide Supermolecules: Coiled-Coil Peptide Structures Templated by d-DNA and l-DNA Triplexes Exhibit Chirality-Independent but Orientation-Dependent Stabilizing Cooperativity. *Chem. Eur. J.* **2020**, *26* (25), 5676-5684. DOI: https://doi.org/10.1002/chem.201905636.
(38) Jin, J.; Baker, E. G.; Wood, C. W.; Bath, J.; Woolfson, D. N.; Turberfield, A. J. Peptide Assembly Directed and Quantified Using Megadalton DNA Nanostructures. *ACS Nano* **2019**, *13* (9), 9927-9935. DOI: 10.1021/acsnano.9b04251.
(39) Novacek, A.; Ugaz, B.; Stephanopoulos, N. Templating Peptide Chemistry with Nucleic Acids: Toward Artificial Ribosomes, Cell-Specific Therapeutics, and Novel Protein-Mimetic Architectures. *Biomacromolecules* **2024**, *25* (7), 3865-3876. DOI: 10.1021/acs.biomac.4c00372.
(40) Seeman, N. C.; Sleiman, H. F. DNA nanotechnology. *Nat. Rev. Mater.* **2017**, *3* (1), 17068. DOI: 10.1038/natrevmats.2017.68.
(41) Zhang, Y.; Pan, V.; Li, X.; Yang, X.; Li, H.; Wang, P.; Ke, Y. Dynamic DNA Structures. *Small* **2019**, *15* (26), 1900228. DOI: https://doi.org/10.1002/smll.201900228.
(42) Zhao, F.; Frandsen, M.; Capodaglio, S.; Sleiman, H. F. DNA-Mediated Peptide Assembly into Protein Mimics. *J. Am. Chem. Soc.* **2024**, *146* (3), 1946-1956. DOI: 10.1021/jacs.3c08984.
(43) Zhao, F.; Sun, Z.; Sleiman, H. F. DNA-Templated Assembly of Metalloprotein Mimics with Hydrolytic Activity. *J. Am. Chem. Soc.* **2025**. DOI: 10.1021/jacs.5c10056.
(44) Rivera, M. Bacterioferritin: Structure, Dynamics, and Protein–Protein Interactions at Play in Iron Storage and Mobilization. *Acc. Chem. Res.* **2017**, *50* (2), 331-340. DOI: 10.1021/acs.accounts.6b00514.
(45) Guo, M.; Gao, M.; Liu, J.; Xu, N.; Wang, H. Bacterioferritin nanocage: Structure, biological function, catalytic mechanism, self-assembly and potential applications. *Biotechnology Advances* **2022**, *61*, 108057. DOI: https://doi.org/10.1016/j.biotechadv.2022.108057.
(46) Crow, A.; Lawson, T. L.; Lewin, A.; Moore, G. R.; Brun, N. E. L. Structural Basis for Iron Mineralization by Bacterioferritin. *J. Am. Chem. Soc.* **2009**, *131* (19), 6808-6813. DOI: 10.1021/ja8093444.

(47) Poppleton, E.; Romero, R.; Mallya, A.; Rovigatti, L.; Šulc, P. OxDNA.org: a public webserver for coarse-grained simulations of DNA and RNA nanostructures. *Nucleic Acids Res.* **2021**, *49* (W1), W491-W498. DOI: 10.1093/nar/gkab324 (acccessed 7/23/2024).
(48) The PyMOL Molecular Graphics System, Version 2.1 Schrödinger, LLC.
(49) Pettersen, E. F.; Goddard, T. D.; Huang, C. C.; Meng, E. C.; Couch, G. S.; Croll, T. I.; Morris, J. H.; Ferrin, T. E. UCSF ChimeraX: Structure visualization for researchers, educators, and developers. *Protein Sci.* **2021**, *30* (1), 70-82. DOI: https://doi.org/10.1002/pro.3943.
(50) Rivera, M. Mobilization of iron stored in bacterioferritin, a new target for perturbing iron homeostasis and developing antibacterial and antibiofilm molecules. *Journal of Inorganic Biochemistry* **2023**, *247*, 112306. DOI: https://doi.org/10.1016/j.jinorgbio.2023.112306.
(51) Honarmand Ebrahimi, K.; Hagedoorn, P.-L.; Hagen, W. R. Unity in the Biochemistry of the Iron-Storage Proteins Ferritin and Bacterioferritin. *Chem. Rev.* **2015**, *115* (1), 295-326. DOI: 10.1021/cr5004908.
(52) Liu, L.; Harmon, E. K.; Craig, J. K.; Yao, H.; Battaile, K. P.; Johnson, D. K.; Subramanian, S.; Van Voorhis, W. C.; Rivera, M.; Lovell, S. Structural Analysis and Inhibitor Modeling of Bacterioferritin From Brucella abortus. *Proteins: Structure, Function, and Bioinformatics n/a* (n/a). DOI: https://doi.org/10.1002/prot.70109.
(53) Sato, D.; Ohtomo, H.; Yamada, Y.; Hikima, T.; Kurobe, A.; Fujiwara, K.; Ikeguchi, M. Ferritin Assembly Revisited: A Time-Resolved Small-Angle X-ray Scattering Study. *Biochem.* **2016**, *55* (2), 287-293. DOI: 10.1021/acs.biochem.5b01152.
(54) Bradley, J. M.; Gray, E.; Richardson, J.; Moore, G. R.; Le Brun, N. E. Protein encapsulation within the internal cavity of a bacterioferritin. *Nanoscale* **2022**, *14* (34), 12322-12331, 10.1039/D2NR01780F. DOI: 10.1039/D2NR01780F.
(55) Kim, M.; Rho, Y.; Jin, K. S.; Ahn, B.; Jung, S.; Kim, H.; Ree, M. pH-Dependent Structures of Ferritin and Apoferritin in Solution: Disassembly and Reassembly. *Biomacromolecules* **2011**, *12* (5), 1629-1640. DOI: 10.1021/bm200026v.
(56) Malone, S. A.; Lewin, A.; Kilic, M. A.; Svistunenko, D. A.; Cooper, C. E.; Wilson, M. T.; Le Brun, N. E.; Spiro, S.; Moore, G. R. Protein-Template-Driven Formation of Polynuclear Iron Species. *J. Am. Chem. Soc.* **2004**, *126* (2), 496-504. DOI: 10.1021/ja036483z.
(57) Wong, S. G.; Tom-Yew, S. A. L.; Lewin, A.; Le Brun, N. E.; Moore, G. R.; Murphy, M. E. P.; Mauk, A. G. Structural and Mechanistic Studies of a Stabilized Subunit Dimer Variant of *Escherichia coli* Bacterioferritin Identify Residues Required for Core Formation. *Journal of Biological Chemistry* **2009**, *284* (28), 18873-18881. DOI: 10.1074/jbc.M901747200 (acccessed 2026/02/26).
(58) Agard, N. J.; Prescher, J. A.; Bertozzi, C. R. A Strain-Promoted [3 + 2] Azide−Alkyne Cycloaddition for Covalent Modification of Biomolecules in Living Systems. *J. Am. Chem. Soc.* **2004**, *126* (46), 15046-15047. DOI: 10.1021/ja044996f.
(59) McLaughlin, C. K.; Hamblin, G. D.; Hänni, K. D.; Conway, J. W.; Nayak, M. K.; Carneiro, K. M. M.; Bazzi, H. S.; Sleiman, H. F. Three-Dimensional Organization of Block Copolymers on "DNA-Minimal" Scaffolds. *J. Am. Chem. Soc.* **2012**, *134* (9), 4280-4286. DOI: 10.1021/ja210313p.
(60) Edwardson, T. G. W.; Lau, K. L.; Bousmail, D.; Serpell, C. J.; Sleiman, H. F. Transfer of molecular recognition information from DNA nanostructures to gold nanoparticles. *Nat. Chem.* **2016**, *8* (2), 162-170. DOI: 10.1038/nchem.2420.
(61) Bujold, K. E.; Hsu, J. C. C.; Sleiman, H. F. Optimized DNA "Nanosuitcases" for Encapsulation and Conditional Release of siRNA. *J. Am. Chem. Soc.* **2016**, *138* (42), 14030-14038. DOI: 10.1021/jacs.6b08369.
(62) Trinh, T.; Liao, C.; Toader, V.; Barłóg, M.; Bazzi, H. S.; Li, J.; Sleiman, H. F. DNA-imprinted polymer nanoparticles with monodispersity and prescribed DNA-strand patterns. *Nat. Chem.* **2018**, *10* (2), 184-192. DOI: 10.1038/nchem.2893.
(63) Edwardson, T. G. W.; Carneiro, K. M. M.; McLaughlin, C. K.; Serpell, C. J.; Sleiman, H. F. Site-specific positioning of dendritic alkyl chains on DNA cages enables their geometry-dependent self-assembly. *Nat. Chem.* **2013**, *5* (10), 868-875. DOI: 10.1038/nchem.1745.
(64) Chidchob, P.; Offenbartl-Stiegert, D.; McCarthy, D.; Luo, X.; Li, J.; Howorka, S.; Sleiman, H. F. Spatial Presentation of Cholesterol Units on a DNA Cube as a Determinant of Membrane Protein-Mimicking Functions. *J. Am. Chem. Soc.* **2019**, *141* (2), 1100-1108. DOI: 10.1021/jacs.8b11898.
(65) Chidchob, P.; Edwardson, T. G. W.; Serpell, C. J.; Sleiman, H. F. Synergy of Two Assembly Languages in DNA Nanostructures: Self-Assembly of Sequence-Defined Polymers on DNA Cages. *J. Am. Chem. Soc.* **2016**, *138* (13), 4416-4425. DOI: 10.1021/jacs.5b12953.
(66) Parida, A.; Mohanty, A.; Raut, R. K.; Padhy, I.; Behera, R. K. Modification of 4-Fold and B-Pores in Bacterioferritin from Mycobacterium tuberculosis Reveals Their Role in Fe2+ Entry and Oxidoreductase Activity. *Inorganic Chemistry* **2023**, *62* (1), 178-191. DOI: 10.1021/acs.inorgchem.2c03156.
(67) Hopp, M.-T.; Schmalohr, B. F.; Kühl, T.; Detzel, M. S.; Wißbrock, A.; Imhof, D. Heme Determination and Quantification Methods and Their Suitability for Practical Applications and Everyday Use. *Analytical Chemistry* **2020**, *92* (14), 9429-9440. DOI: 10.1021/acs.analchem.0c00415.
(68) Stein, D.; Jartoux, B.; Dror, S.; Uebe, R.; Koubková-Yu, T. C.-T.; Zalk, R.; Shahar, A.; Zarivach, R.; Frank, G. A. The assembly rules guiding hetero-oligomeric bacterioferritin organization and their evolutionary signature. *Proc. Natl Acad. Sci.* **2026**, *123* (5), e2504561123. DOI: doi:10.1073/pnas.2504561123.
(69) Pullin, J.; Wilson, M. T.; Clémancey, M.; Blondin, G.; Bradley, J. M.; Moore, G. R.; Le Brun, N. E.; Lučić, M.; Worrall, J. A. R.; Svistunenko, D. A. Iron Oxidation in Escherichia coli Bacterioferritin Ferroxidase Centre, a Site Designed to React Rapidly with H2O2 but Slowly with O2. *Angew. Chem. Int. Ed.* **2021**, *60* (15), 8361-8369. DOI: https://doi.org/10.1002/anie.202015964.
(70) Jobichen, C.; Ying Chong, T.; Rattinam, R.; Basak, S.; Srinivasan, M.; Choong, Y. K.; Pandey, K. P.; Ngoc, T. B.; Shi, J.; Angayarkanni, J.; et al. Bacterioferritin nanocage structures uncover the biomineralization process in ferritins. *PNAS Nexus* **2023**, *2* (7). DOI: 10.1093/pnasnexus/pgad235 (acccessed 3/1/2026).

(71) Praetorius, F.; Leung, P. J. Y.; Tessmer, M. H.; Broerman, A.; Demakis, C.; Dishman, A. F.; Pillai, A.; Idris, A.; Juergens, D.; Dauparas, J.; et al. Design of stimulus-responsive two-state hinge proteins. *Science* **2023**, *381* (6659), 754-760. DOI: doi:10.1126/science.adg7731.
(72) Pillai, A.; Idris, A.; Philomin, A.; Weidle, C.; Skotheim, R.; Leung, P. J. Y.; Broerman, A.; Demakis, C.; Borst, A. J.; Praetorius, F.; et al. De novo design of allosterically switchable protein assemblies. *Nature* **2024**, *632* (8026), 911-920. DOI: 10.1038/s41586-024-07813-2.
(73) Yu, B.; Liu, J.; Cui, Z.; Wang, C.; Chen, P.; Wang, C.; Zhang, Y.; Zhu, X.; Zhang, Z.; Li, S.; et al. De novo design of light-responsive protein–protein interactions enables reversible formation of protein assemblies. *Nat. Chem.* **2025**, *17* (12), 1910-1919. DOI: 10.1038/s41557-025-01929-2.
(74) Machinek, R. R. F.; Ouldridge, T. E.; Haley, N. E. C.; Bath, J.; Turberfield, A. J. Programmable energy landscapes for kinetic control of DNA strand displacement. *Nat. Commun.* **2014**, *5* (1), 5324. DOI: 10.1038/ncomms6324.
(75) Simmel, F. C.; Yurke, B.; Singh, H. R. Principles and Applications of Nucleic Acid Strand Displacement Reactions. *Chem. Rev.* **2019**, *119* (10), 6326-6369. DOI: 10.1021/acs.chemrev.8b00580.
(76) Lapteva, A. P.; Sarraf, N.; Qian, L. DNA Strand-Displacement Temporal Logic Circuits. *J. Am. Chem. Soc.* **2022**, *144* (27), 12443-12449. DOI: 10.1021/jacs.2c04325.
(77) Ulas, G.; Lemmin, T.; Wu, Y.; Gassner, G. T.; DeGrado, W. F. Designed metalloprotein stabilizes a semiquinone radical. *Nat. Chem.* **2016**, *8* (4), 354-359. DOI: 10.1038/nchem.2453.
(78) Luo, Q.; Hou, C.; Bai, Y.; Wang, R.; Liu, J. Protein Assembly: Versatile Approaches to Construct Highly Ordered Nanostructures. *Chem. Rev.* **2016**, *116* (22), 13571-13632. DOI: 10.1021/acs.chemrev.6b00228.
(79) Wang, S.; Favor, A.; Kibler, R. D.; Lubner, J. M.; Borst, A. J.; Coudray, N.; Redler, R. L.; Chiang, H. T.; Sheffler, W.; Hsia, Y.; et al. Bond-centric modular design of protein assemblies. *Nature Materials* **2025**, *24* (10), 1644-1652. DOI: 10.1038/s41563-025-02297-5.
(80) McLaughlin, C. K.; Hamblin, G. D.; Sleiman, H. F. Supramolecular DNA assembly. *Chemical Society Reviews* **2011**, *40* (12), 5647-5656, 10.1039/C1CS15253J. DOI: 10.1039/C1CS15253J.
(81) Fu, J.; Liu, M.; Liu, Y.; Woodbury, N. W.; Yan, H. Interenzyme Substrate Diffusion for an Enzyme Cascade Organized on Spatially Addressable DNA Nanostructures. *J. Am. Chem. Soc.* **2012**, *134* (12), 5516-5519. DOI: 10.1021/ja300897h.
(82) Ma, Y.; Winegar, P. H.; Figg, C. A.; Ramani, N.; Anderson, A. J.; Ngo, K.; Ahrens, J. F.; Chellam, N. S.; Kim, Y. J.; Mirkin, C. A. DNA-Regulated Multi-Protein Complement Control. *J. Am. Chem. Soc.* **2024**, *146* (48), 32912-32918. DOI: 10.1021/jacs.4c11315.
(83) Wamhoff, E.-C.; Ronsard, L.; Feldman, J.; Knappe, G. A.; Hauser, B. M.; Romanov, A.; Case, J. B.; Sanapala, S.; Lam, E. C.; Denis, K. J. S.; et al. Enhancing antibody responses by multivalent antigen display on thymus-independent DNA origami scaffolds. *Nat. Commun.* **2024**, *15* (1), 795. DOI: 10.1038/s41467-024-44869-0.
(84) Asohan, J.; Fakih, H. H.; Das, T.; Sleiman, H. F. Control of the Assembly and Disassembly of Spherical Nucleic Acids Is Critical for Enhanced Gene Silencing. *ACS Nano* **2024**, *18* (5), 3996-4007. DOI: 10.1021/acsnano.3c05940.
(85) Cutler, J. I.; Auyeung, E.; Mirkin, C. A. Spherical Nucleic Acids. *J. Am. Chem. Soc.* **2012**, *134* (3), 1376-1391. DOI: 10.1021/ja209351u.
(86) Banga, R. J.; Chernyak, N.; Narayan, S. P.; Nguyen, S. T.; Mirkin, C. A. Liposomal Spherical Nucleic Acids. *J. Am. Chem. Soc.* **2014**, *136* (28), 9866-9869. DOI: 10.1021/ja504845f.
(87) Mirkin, C. A.; Petrosko, S. H. Inspired Beyond Nature: Three Decades of Spherical Nucleic Acids and Colloidal Crystal Engineering with DNA. *ACS Nano* **2023**, *17* (17), 16291-16307. DOI: 10.1021/acsnano.3c06564.
(88) Mutter, M. Four decades, four places and four concepts. *Chimia (Aarau)* **2013**, *67* (12-13), 868-873. DOI: 10.2533/chimia.2013.868 From NLM.

Acknowledgements

This work was funded by the Natural Science and Engineering Research Council of Canada (NSERC), Canada Foundation for Innovation (CFI), and Fonds de Recherche du Québec – Nature et technologies (FRQNT). H.F.S. is thankful to the Canada Research Chairs Program and is a Cottrell Scholar of the Research Corporation.

Author and Affiliations

Department of Chemistry and Centre de Recherche en Biologie Structurale, McGill University, 801 Sherbrooke St. W., Montreal, QC, Canada

Fangzhou Zhao, Daniel Saliba, Ziyi Sun, Trishalina Das, Jathavan Asohan, Yihao Wu, and Hanadi F. Sleiman

Department of Biochemistry and Centre de Recherche en Biologie Structurale, McGill University, 3649 Promenade Sir William Osler, Montreal, QC, Canada

Tianxiao Yang and Alba Guarné

Contributions

F.Z. designed and performed experiments and wrote the manuscript. T.Y. performed cryo-EM characterisation and analyzed the data. D.S., Z.S., and Y.W. collected the AFM images. T.D. collected the DLS data. J.A. synthesized amphiphilic DNA strands for SNA assembly. A.G. supervised the cryo-EM experiments and edited the manuscript. H.F.S. supervised the project, reviewed, and edited the manuscript.

Supplementary Files

This is a list of supplementary files associated with this preprint. Click to download.

- SupportingInformation.pdf
- RigidifiedDNAcubewithsplint2T.gif
- NormalDNAcube.gif